Significantly Enhancing Supercapacitive Performance of Nitrogen-doped Graphene Nanosheet Electrodes by Phosphoric Acid Activation

Ping Wang,[†] Haili He,[†,‡] Xiaolong Xu,[†] and Yongdong Jin*,[†]

[†]State Key Laboratory of Electroanalytical Chemistry, Changchun Institute of Applied Chemistry, Chinese Academy of Sciences, Changchun 130022, People's Republic of China

[‡]Graduate University of the Chinese Academy of Sciences, Beijing 100039, People's Republic of China

Ⓢ *Supporting Information*

ABSTRACT: In this work, we present a new method to synthesize the phosphorus, nitrogen contained graphene nanosheets, which uses dicyandiamide to prevent the aggregation of graphene oxide and act as the nitrogen precursor, and phosphoric acid (H_3PO_4) as the activation reagent. We have found that through the H_3PO_4 activation, the samples exhibit the remarkably enhanced supercapacitive performance, and depending on the amount of H_3PO_4 introduced, the specific capacitance of the samples is gradually increased from 7.6 to 244.6 F g^{-1}. Meanwhile, the samples also exhibit the good rate capability and excellent stability (up to 10 000 cycles). Through the transmission electron microscopy, high-resolution transmission electron microscopy, X-ray diffraction, X-ray photoelectron spectroscopy and Brunauer−Emmett−Teller analyses, H_3PO_4 treatment induced large pore volume and phosphorus related function groups in the product are assumed to response for the enhancement.

KEYWORDS: *Graphene, supercapacitors, nitrogen, phosphorus, nanostructures*
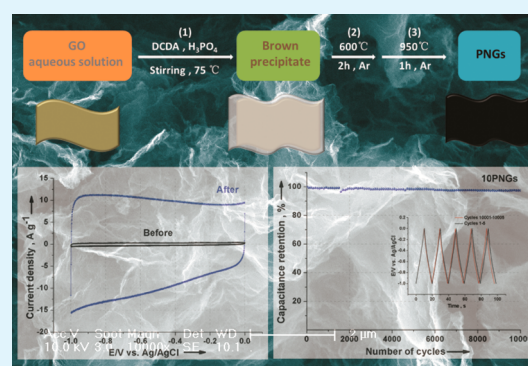
1. INTRODUCTION

Supercapacitors (SCs) as an important class of energy storage devices have attracted worldwide attention due to its merits of high powder density, long-lifetime up to million cycles, and fast charge/discharge rates.[1−5] Most SC electrodes so far employ carbon-based materials such as active carbon,[6] mesoporous carbon[7] or carbon nanotube[8] nanostructures, which show good stability but moderate capacitance. Recently, a new carbon-based nanomaterial, graphene, due to its high specific surface area (theoretical value of 2630 m^2 g^{-1}), extraordinary intrinsic electrical conductivity, as well as strong mechanical strength and excellent chemical stability,[9−14] has been considered as an ideal candidate for SC electrodes. Ruoff et al. pioneered the work of this area, in which the graphene-based supercapacitor (GSC) offers a specific capacitance of up to 130 F g^{-1} and 100 F g^{-1} in aqueous KOH and organic electrolyte, respectively.[15] However, the restacking of graphene inevitably decreases the performance of GSCs. Attempts to solve the problem through KOH activation to generate micorpores in the product,[16] laser scribing[17] or other methods[18] to form a three-dimensional (3D) graphene framework have been proven to effectively enhance the performance of GSCs.

Besides the physical restructuring, chemical modification of graphene is another way to further improve the supercapacitive performance of GSCs. The integration of graphene nanosheets with nanosized metal oxides such as RuO$_2$, MnO$_2$ and NiO or conducting polymers[19−22] can significantly increase the specific capacitance (*Cs*) of the composites. However, the short cycle life and poor rate capability limit its practical application. Recently, heteroatom doping has been preliminarily proven to be an effective method to enhance the SC performance of graphene. Kang and Choi et al. reported that nitrogen-doped graphene nanosheets (NGs) produced by plasma treatment exhibits four times larger capacitance than pristine counterparts, while maintaining other essential properties, and they ascribe the enhancement to the increasing of the binding energy of N-configuration with ions in the electrolyte.[23] Since then, other NGs nanostructures have been prepared and also displays high-performance for SCs.[24−26]

Herein, we report that phosphoric acid (H_3PO_4) can be used to activate NGs for SCs. The Brunauer−Emmett−Teller (BET) specific surface area (SSA), pore volume and phosphorus-related functional groups of the product could be readily controlled by the amount of H_3PO_4 added. Through the H_3PO_4 activation, the resultant phosphorus, nitrogen contained graphene nanosheets (PNGs) exhibit significantly enhanced electrochemical capacitance, as well as good rate capability and excellent stability.

2. EXPERIMENTAL SECTION

2.1. Chemicals. Graphite powder was purchased from Alfa Aesar. Dicyandiamide (DCDA) (99%), phosphoric acid (H_3PO_4) (>99.999% trace metals basis), potassium hydroxide (KOH) (≥85%) and Nafion (~5 wt %) 117 solution were purchased from Sigma-Aldrich. All chemicals were used as received and without any further purification.

2.2. Synthesis of Phosphoric Acid Activated Nitrogen-Doped Graphene. Graphite oxide was prepared from natural graphite powder by a modified Hummers method.[27] Two grams of DCDA together with different amount of H_3PO_4 (0, 0.1, 0.5, 1.0 g) was dissolved into 100 mL of graphene oxide (0.25 mg mL^{-1}) at room temperature. After that, the solution was heated to 75 °C under vigorous stirring to evaporate the water. The obtained brown precipitate was then transferred into the tube furnace and heated under the prefixed procedure (see the Supporting Information) with the protection of argon (30 mL min^{-1}).

2.3. Electrochemical Measurements. The capacitance properties of the samples were evaluated through the three-electrode systems by using a CHI 660E electrochemical workstation. A 6 M KOH aqueous solution with the protection of nitrogen flow is used as the electrolyte. Ag/AgCl (KCl 3M) and Pt wire are used as the reference and counter electrode, respectively. A glassy carbon (GC) electrode is used as the working electrode. Before use, it was polished using 1.0 and 0.05 mm alumina slurries, sequentially, and followed by rinse and sonication in DI-water for 5 min. For making the electrodes, 1 mg of active material was homogeneously dispersed into 0.5 mL of acetone by sonication. Then, 10 μL aliquot of the solution was pipetted onto the GC electrode, and the loading mass for all the samples on the electrode is 0.02 mg. After the evaporation of acetone, 5 μL of Nafion (0.5 wt %) solution was covered on the top of the GC electrode. Finally, it was transferred into desiccator to dry before characterization. Cyclic voltammetries (CVs) were carried in the potential range from −1.0 V to 0 V (vs. Ag/AgCl reference electrode). Galvanostatic charge−discharge measurements were performed by cycling the voltage from −1.0 V to 0 V (vs Ag/AgCl reference electrode) at different current densities (0.1, 0.2, 0.5, 1.0, 2.0, 5.0, 10.0 A g^{-1}).

The specific capacitance Cs (F g^{-1}) of the samples was calculated based on the galvanostatic charge−discharge curves according to the following equation:

$$Cs = I / \left(\left(\frac{dV}{dt} \right) m \right)$$

where I is the applied current density, m is the mass of active electrode material, and dV/dt is the slope of the galvanostatic discharge curve.

2.4. Characterization. The morphologies of the samples and energy dispersive X-ray (EDX) analysis were obtained on an XL 30 ESEM FEG field emission scanning electron microscope (FESEM; FEI Company). Transmission electron microscopy (TEM), high-resolution TEM (HRTEM), and elemental mapping measurements were carried out by using a FEI TECNAI F20 EM with an accelerating voltage of 200 kV equipped with an energy dispersive spectrometer. TEM samples were prepared by placing a drop of the solution with sample on a carbon-coated copper grid and drying under ambient conditions. X-ray photoelectron spectroscopy (XPS) measurements were recorded on a Thermo VG Scientific ESCALAB 250 spectrometer using monochromatized Al Kα excitation. X-ray diffraction patterns were recorded by a D8 ADVANCE (BRUKER) diffractometer with Cu Kα radiation ($λ$ = 1.540 56 Å) in the range of 12−60° ($2θ$). Raman measurements were performed on a J-Y T64000 Raman spectrometer with 514.5 nm wavelength incident laser light. The specific surface area, pore volume and pore size distribution were obtained on ASAP 2020 (Micromeritics) and calculated by the Brunauer−Emmett−Teller (BET) and Barrett−Joyner−Halenda (BJH) methods, respectively.

3. RESULTS AND DISCUSSION

Scheme 1 represents the standard procedure for the synthesis of PNGs. The synthesis involves three steps: (1) dicyandiamide

Scheme 1. Schematic Illustration of the Protocol for the Homogeneous Mixing of DCDA, H_3PO_4 and GO; Polymerization of DCDA into C_3N_4; and Further Decomposition of C_3N_4 and Thermal Reduction of GO into PNGs
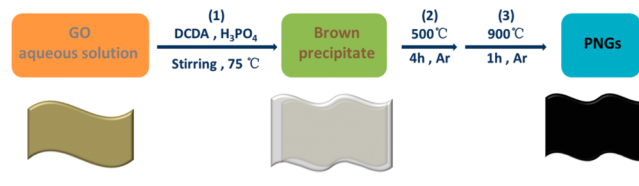
(DCDA) and H_3PO_4 were dissolved into graphene oxide (GO) aqueous solution under vigorous stirring. After that, the mixed solution was heated to 75 °C to evaporate the H_2O to get the brown precipitate. During this process, DCDA, phosphoric acid and GO would be homogeneously mixed; (2) the obtained precipitate was then transferred into the tube furnace and heated at 500 °C under the protection of argon (Ar), to induce the thermal polymerization of DCDA to form C_3N_4 on the surface of GO;[28] (3) finally, the heating temperature was raised to 900 °C to decompose C_3N_4, thermally reduce GO into graphene and complete the doping process. In the synthesis, DCDA acts as both spacers to prevent the aggregation of GO nanosheets during annealing process and nitrogen precursor, while H_3PO_4 acts as the phosphorus precursor, the reactant to generate nanopores and further increase SSA of the products. We found that H_3PO_4 treatment markedly enhances super-capacitive performance of the NGs electrodes and the enhancement is highly dependent on the amount of H_3PO_4 introduced. According to the amount of H_3PO_4 introduced during the synthesis, the obtained representative samples in this study are denoted briefly as NGs, 1PNGs, 5PNGs and 10PNGs, respectively.

The detailed structure information of the products was characterized by scanning electron microscopy (SEM) and transmission electron microscopy (TEM). From the SEM images (see the Supporting Information, Figure S-1), all the samples possess two-dimensional sheet-like crumpled morphology, and the samples synthesized with the addition of H_3PO_4 display more wrinkled nanostructures. Energy-dispersive X-ray spectroscopy (EDS) measurements (see the Supporting Information, Figure S-2) show the elemental composition and atom ratio of different samples, and the results indicate that all the samples contain no-impurities except of Si resulting from the substrate. Further TEM investigation (see the Supporting Information, Figure S-3) reveals that all the samples exhibit the wrinkled sheet-like nanostructures. The results imply that the introduction of DCDA and H_3PO_4 both play the role to effectively prevent the aggregation of graphene sheets during the annealing process.

Figure 1 shows the detailed structure information of the representative sample, 10PNGs. SEM (Figure 1a) and TEM (Figure 1b) images clearly show the existence of wrinkled structures in 10PNGs; further high-resolution TEM (HRTEM) (Figure 1c) investigation indicates that the sample is in a multilayer form, which is well consistent with the result of the selected area electron diffraction (SAED) pattern (inset of Figure 1c). Elemental mapping measurements (Figure 1d−g) confirm the homogeneous dispersion of nitrogen, oxygen and phosphorus elements in the graphene nanosheet.
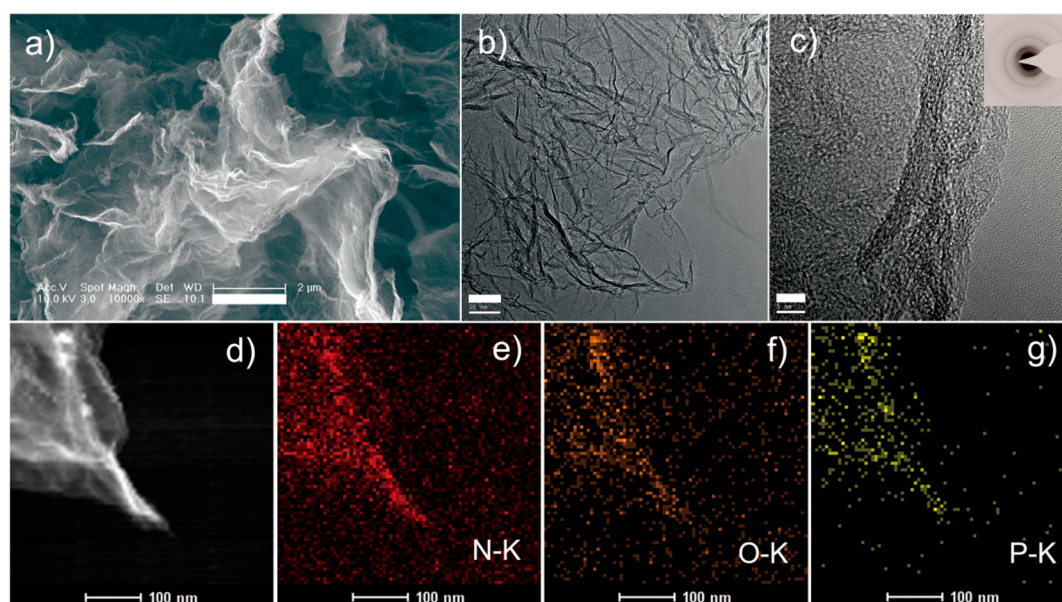
Figure 1. (a) Low-magnification SEM image of the 10PNGs, scale bar: 2 μm. (b) TEM image of the 10PNGs showing the wrinkled structures, scale bar: 50 nm. (c) HRTEM image of the 10PNGs that demonstrates the multilayer structure, scale bar: 5 nm. Inset is the SAED pattern of the corresponding area. (d) Dark-field TEM image of the 10PNGs, and corresponding nitrogen (e), oxygen (f) and phosphorus (g) elemental-mapping images, scale bar: 100 nm.
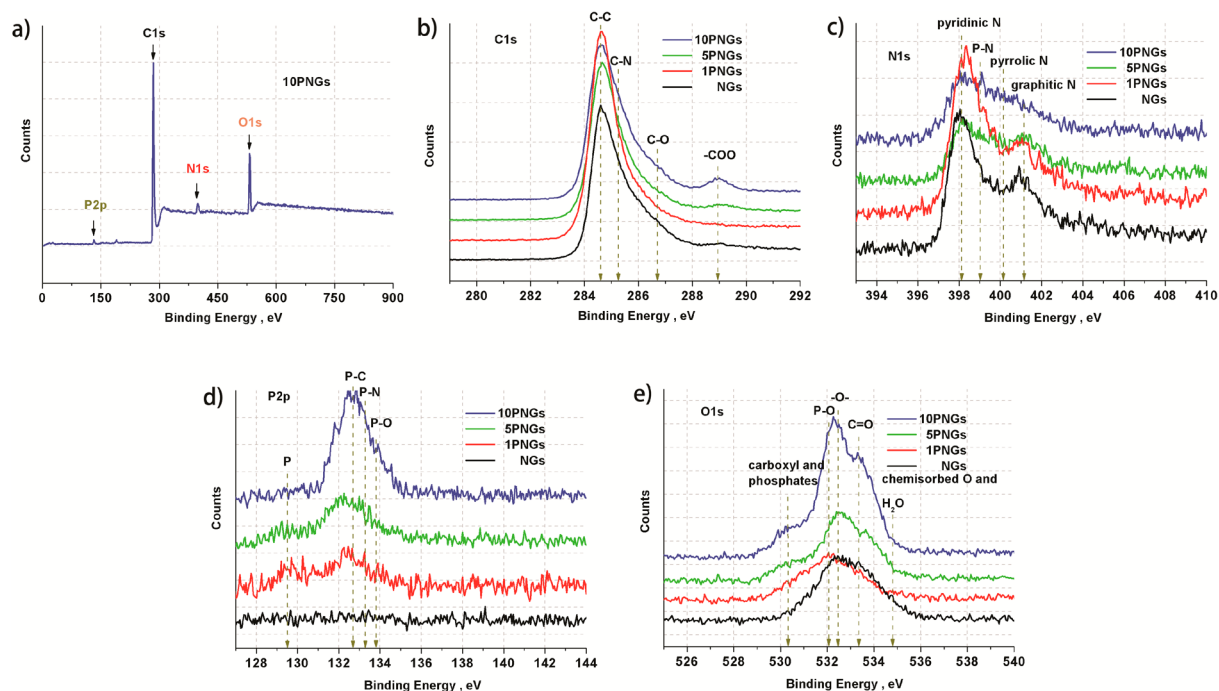

Figure 2. (a) Full survey of XPS spectroscopy of the 10PNGs clearly showing the existence of elements of carbon, nitrogen, oxygen and phosphorus; (b) C1s, (c) N1s, (d) P2p and (e) O1s spectra of NGs, 1PNGs, 5PNGs and 10PNGs, respectively.

X-ray photoelectron spectroscopy (XPS) analyses were further carried out to get the detailed bonding information and to quantify the elemental atom ratios in the samples. Figure 2a shows the full XPS survey of the 10PNGs, and the obvious peaks observed at 132.3, 284.9, 399.2, and 532.2 eV corresponding to P 2p, C 1s, N 1s, and O 1s, respectively. High-resolution C 1s XPS spectra (Figure 2b) reveal that besides the predominant peak at 284.6 attributed to C−C bonding, an obvious tail toward higher binding energy, which is thought to be the result of C−N bonding, C−O bonding, and

C−P or C−O−P bonding,[29] is observed. However, it is worth noting that for C 1s spectrum, phosphorus cannot be clearly identified, as the binding energy (BE) of C−O−P bonding is similar to that of ether, whereas the BE of phosphonates is between graphitic and oxygenate carbon.[30−32]

The N 1s spectra (Figure 2c) demonstrate that N atoms are inserted into the graphene basal plane in the form of "pyridinic", "pyrrolic" and "graphitic" N. Furthermore, it is clearly seen that the component of P—N bonding at 399.0 eV[29] is gradually increased as the phosphorus doping level

Table 1. Comparison of N, O and P Atom Percentage Obtained from XPS Analysis, Surface Area, and Pore Volume of Different Samples

sample	N [At. %]	O [At. %]	P [At. %]	$S_{BET}{}^a$ [m^2 g^{-1}]	$V_{pore}{}^b$ [cm^3 g^{-1}]
NGs	5.96 ± 0.85	7.81 ± 0.52	N/A	45.2	0.09
1PNGs	7.46 ± 0.34	5.00 ± 0.41	0.57 ± 0.25	379.6	0.55
5PNGs	4.78 ± 0.72	6.26 ± 1.22	1.17 ± 0.10	1090.2	1.34
10PNGs	4.81 ± 0.89	14.46 ± 2.74	1.57 ± 0.18	1040.6	1.84

^{a}Specific surface area calculated from multiple BET method. ^{b}Pore volume at $P/P_0 = 0.97$.
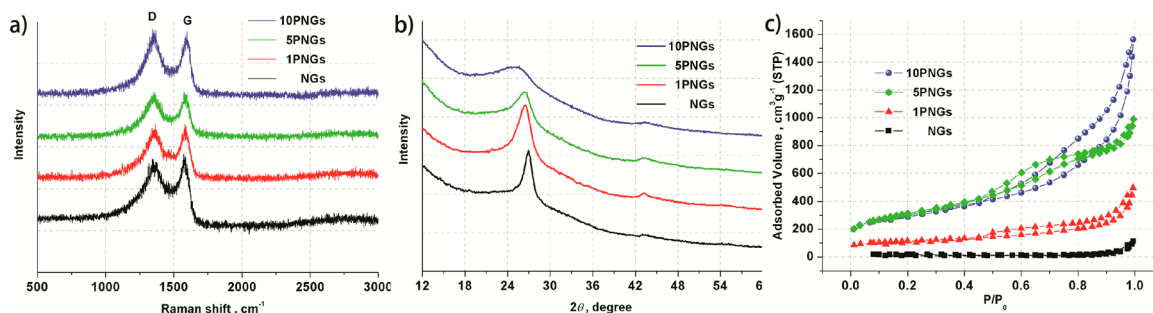
Figure 3. (a) Raman spectra, (b) XRD patterns and (c) High-resolution, low-pressure N$_2$ isotherms at 77.4 K of different samples.
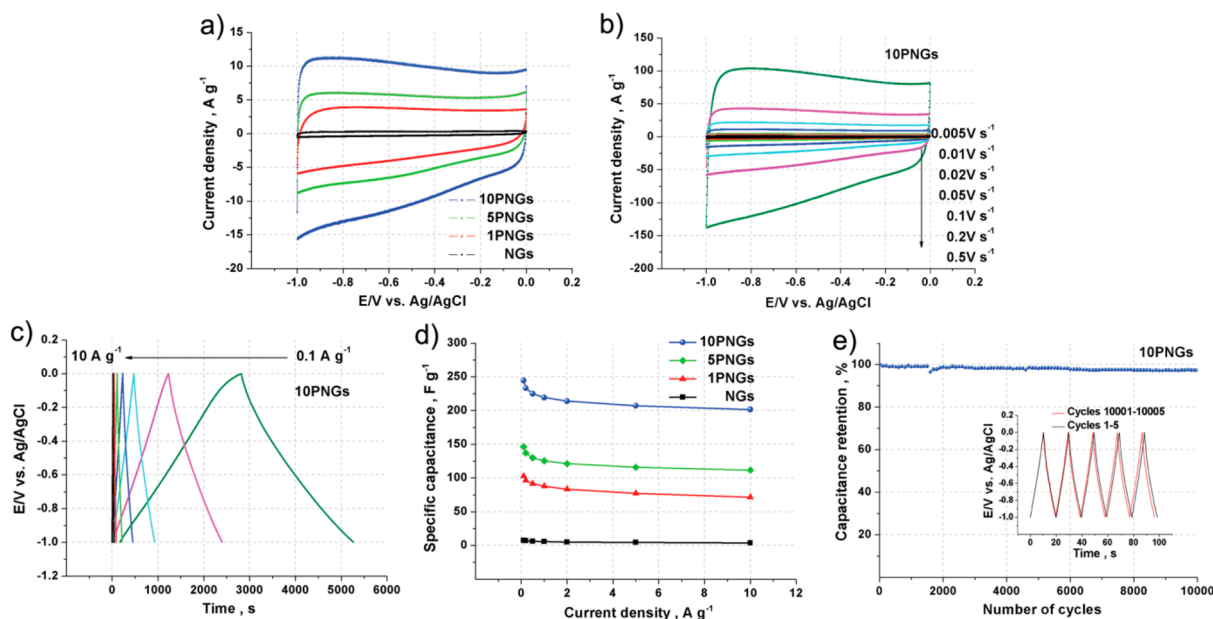
Figure 4. (a) CV curves of different samples in 6 M KOH with scan rate of 50 mV s^{-1}. All curves display the nearly rectangular shape demonstrating the good capacitive behavior. (b) CV curves of the 10PNGs for different scan rates from 0.005 to 0.5 V s^{-1}. (c) Galvanostatic charge/discharge curves of the 10 PNGs under different constant currents densities (0.1, 0.2, 0.5, 1.0, 2.0, 5.0, 10.0 A g^{-1}). (d) Specific capacitance dependence of different samples on constant currents densities. (e) Capacitance retention ratio of the 10PNGs as a function of number of galvanostatic charge/discharge cycles under constant current density of 20.0 A g^{-1}. The inset is the comparison of galvanostatic charge/discharge curves of first five cycles with last cycles from 10 001 to 10 005, demonstrating the excellent stability of the 10PNGs as the SC electrode.

increased. A similar trend is also observed for the P−N bonding (133.3 eV)[29] in the P 2p spectra (Figure 2d). In addition, a trace amount of elemental phosphorus is observed, which is consistent with the results reported by Puziy et al.[32] For the O 1s XPS spectra (Figure 2e), it can be seen that as the phosphorus doping level increased, the peak at 530.3 eV corresponding to carboxyl and phosphates[32] gradually increases, and the −O− bond (532.5 eV), P—O bonding (532.1 eV) and C=O bonding (533.3 eV)[29] are also observed. Combined with all above analysis and previous studies,[32] we speculate that the phosphorus in graphene nanosheets is in the form of phosphate PO$_4$/polyphosphate (PO$_3$)$_n$ functional

groups, as further evidenced by the increasing of both phosphorus and oxygen content with the increasing of amount of H$_3$PO$_4$ added during the synthesis (Table 1).

The D/G band ratio in the Raman spectra (Figure 3a) is increased from 0.95 to 1.02, demonstrating that more defects are formed as the increasing of amount of H$_3$PO$_4$ introduced.[33,34] Figure 3b displays the X-ray diffraction (XRD) results of all the samples. As shown, all the samples exhibit two diffraction peaks at ∼26.0° and 43.2°, corresponding to {002} and {100} planes of graphene, respectively. Furthermore, with the increasing of the amount of H$_3$PO$_4$ introduced, the peak attributed to {002} plane dramatically

decreased and become broader, which demonstrates that the addition of H_3PO_4 may inhibit the stacking effect or reduce the domain size of graphene. Interestingly, the peak gradually shifts from 26.9° to 25.2°; this change may be attribute to the introduction of phosphate PO_4/polyphosphate $(PO_3)_n$ functional groups by the H_3PO_4 treatment.

To further explore the structural change of the samples, high-resolution nitrogen adsorption/desorption measurements were carried out. Figure 3c shows the linear plots of the nitrogen isotherms of the four different samples, and the type IV isotherms with distinct hysteresis loops for 1PNGs, 5PNGs and 10PNGs clearly reveal the existence of nanopore structures, whereas for NGs, no such characteristic was observed. The SSA and pore volume of different samples are summarized in Table 1. As clearly shown, increasing the amount of H_3PO_4 under certain amounts during the synthesis could significantly increase both the SSA and pore volume, but more addition leads to no obvious increase of SSA (cf. 5PNGs and 10PNGs). The results clearly demonstrate that the H_3PO_4 plays two roles on the restructuring of NGs: one is to further inhibit the restacking of NGs, as also proved by SEM and XRD results; whereas the other is to generate nanopores in 3D graphene nanosheets, which is confirmed by the results of the pore size distribution (see the Supporting Information, Figure S-4) with average pore width 5.8, 4.9 and 7.0 nm for 1PNGs, 5PNGs and 10PNGs, respectively.

The electrochemical performance of the four different samples for potential application as SC electrodes was evaluated in a three-electrode system, where a specific sample deposited on a glass carbon electrode was used as a working electrode; Ag/AgCl and Pt wire were used as reference and counter electrodes, respectively. Figure 4a shows the cyclic voltammetry (CV) curves of the different samples in 6 M KOH at a scan rate of 50 mV s^{-1}. It can be seen that all the CV curves exhibit the nearly rectangular shape over the range from −1.0 to 0 V indicates the standard electrochemical double-layers capacitive behavior. Interestingly, the current density is increased as the increasing of the amount of H_3PO_4 added. Figure 4b shows CV curves of the 10PNGs for different scan rates, and it can be seen that even at the large scan rate of 0.5 V s^{-1}, the CV curves still exhibit a nearly rectangular shape. The other samples exhibit the similar behavior (see the Supporting Information, Figure S-5). The galvanostatic charge/discharge curves of the 10PNGs at different current densities from 0.1 to 10.0 A g^{-1} are shown in Figure 4c; for clarity, magnification of galvanostatic charge/discharge curves of the 10PNGs at current densities of 1.0, 2.0, 5.0 and 10.0 A g^{-1} are shown in Figure S-6 (see the Supporting Information). The Cs under the current densities of 0.1, 0.2, 0.5, 1.0, 2.0, 5.0 and 10.0 A g^{-1} calculated from the discharge curves are 244.6, 233.3, 224.9, 219.2, 213.9, 207.1 and 201.5 F g^{-1}, respectively. Only a slight decrease is observed for the Cs of the 10PNGs as the increasing of the current density, demonstrating its good rate capability as SC electrode. Figure 4d represents the Cs of different samples as a function of current densities. The results clearly show that, under all current densities, the Cs significantly increases as the increasing of the amount of H_3PO_4 added, with values of 7.6, 102.8, 146.4 and 244.6 F g^{-1} for NGs, 1PNGs, 5PNGs and 10PNGs at a current density of 0.1 A g^{-1}, respectively; whereas the Cs calculated from CV curves is 7.8, 87.9, 125.8 and 218.7 F g^{-1} for NGs, 1PNGs, 5PNGs and 10PNGs with a scan rate of 0.005 V s^{-1}, which is slightly lower than that calculated from the galvanostatic charge/discharge curves, and the change of

capacitance versus scan rate for all the samples is shown in Figure S-7 (see the Supporting Information). For comparison, we also synthesized reduced graphene oxide (RGO) without nitrogen doping by thermally reduction of graphene oxide using the same heat procedure but without introducing DCDA and H_3PO_4, and the Cs of RGO calculated from CV and galvanostatic charge/discharge curve (Supporting Information, Figure S-8) is 14.8 and 32.2 F g^{-1}, respectively, which is comparable with that of NGs. Furthermore, the rate capability is also enhanced with the same trend as Cs. When the current density is increased from 0.1 to 10 A g^{-1}, there are still 51.3, 69.7, 76.4 and 82.4% of capacitance kept for NGs, 1PNGs, 5PNGs and 10PNGs, respectively. The results indicate well potential application of the 10PNGs for SCs.

The electrochemical stability of SC electrode is another key issue for the practical application; therefore, a galvanostatic charge/discharge technique was performed to evaluate the stability of the 10PNG electrode under the current density of 20.0 A g^{-1} (Figure 4e). The Cs of the 10PNG electrode was maintained 97.4 % of its original capacity, which only decreases from 196.8 to 191.6 F g^{-1}, after 10 000 cycles. The inset of Figure 3e shows the comparison of galvanostatic charge/discharge curves of first five cycles with last cycles from 10 001 to 10 005, and no obvious change was observed, demonstrating the excellent stability for the 10PNGs as SC electrode.

The results show clearly that H_3PO_4 activation induces significant enhancement of supercapacitive performance of the NGs electrodes, and we tentatively attribute the effect to both the increasing of pore volume and successful chemical modification by phosphorus-containing functional groups in the products. The large pore volume is thought to facilitate for the fast ion-diffusion and possess the low transfer resistance of ions, which will result in the good capacity of the product; while the phosphorus-containing functional groups may have the positive effect on increasing the capacitive performance; however, the mechanism is yet to be fully understood.

4. CONCLUSION

In conclusion, we have proven that H_3PO_4 can be used to active NGs to significantly enhance their supercapacitive performance. The H_3PO_4 treatment induced structure change of NGs including pore volume and formation of phosphate PO_4/polyphosphate $(PO_3)_n$ functional groups have been considered to be the key factors for the enhancement. This H_3PO_4 activation method may pave a new way to further increasing the performance of graphene-based SC electrodes for the practical applications.

■ ASSOCIATED CONTENT

Ⓢ Supporting Information

Heating procedure for the synthesis of samples; low-magnification SEM images, EDS spectra, TEM images, pore size distribution, galvanostatic charge/discharge of different samples, CV curves of NGs, 1PNGs and 5PNGs; magnification of galvanostatic charge/discharge curves of the 10PNGs at current densities of 1.0, 2.0, 5.0, 10.0 A g^{-1}; specific capacitance dependence of different samples on scan rate; comparison of CV and galvanostatic charge/discharge curves of RGO, NGs and 1PNGs. This material is available free of charge via the Internet at http://pubs.acs.org.

■ AUTHOR INFORMATION

Corresponding Author

* Yongdong Jin. Fax: 86-431-8526 2661. Tel: 86-431-8526 2661. E-mail: ydjin@ciac.ac.cn.

Author Contributions

The paper was written through contributions of all authors. All authors have given approval to the final version of the paper.

Notes

The authors declare no competing financial interest.

■ REFERENCES

(1) Miller, J. R.; Simon, P. *Science* **2008**, *321*, 651−652.

(2) Simon, P.; Gogotsi, Y. *Nat. Mater.* **2008**, *7*, 845−854.

(3) Frackowiak, E.; Béguin, F. *Carbon* **2001**, *39*, 937−950.

(4) Aricò, A. S.; Bruce, P.; Scrosati, B.; Tarascon, J. M.; Van Schalkwijk, W. *Nat. Mater.* **2005**, *4*, 366.

(5) Kötz, R.; Carlen, M. *Electrochim. Acta* **2000**, *45*, 2483−2498.

(6) Jurewicz, K.; Babel, K.; Ziolkowski, A.; Wachowska, H. *Electrochim. Acta* **2003**, *48*, 1491−1498.

(7) Fuertes, A. B.; Lota, G.; Centeno, T. A.; Frackowiak, E. *Electrochim. Acta* **2005**, *50*, 2799−2805.

(8) Futaba, D. N.; Hata, K.; Yamada, T.; Hiraoka, T.; Hayamizu, Y.; Kakudate, Y.; Tanaike, O.; Hatori, H.; Yumura, M.; Iijima, S. *Nat. Mater.* **2006**, *5*, 987−994.

(9) Novoselov, K. S.; Geim, A. K.; Morozov, S. V.; Jiang, D.; Zhang, Y.; Dubonos, S. V.; Grigorieva, I. V.; Firsov, A. A. *Science* **2004**, *306*, 666−669.

(10) Geim, A. K.; Novoselov, K. S. *Nat. Mater.* **2007**, *6*, 183−191.

(11) Zhang, Y. B.; Tan, Y. W.; Stormer, H. L.; Kim, P. *Nature* **2005**, *438*, 201−204.

(12) Castro Neto, A. H.; Guinea, F.; Peres, N. M. R.; Novoselov, K. S.; Geim, A. K. *Rev. Mod. Phys.* **2009**, *81*, 109−162.

(13) Novoselov, K. S.; Geim, A. K.; Morozov, S. V.; Jiang, D.; Katsnelson, M. I.; Grigorieva, I. V.; Dubonos, S. V.; Firsov, A. A. *Nature* **2005**, *438*, 197−200.

(14) Berger, C.; Song, Z. M.; Li, X. B.; Wu, X. S.; Brown, N.; Naud, C.; Mayou, D.; Li, T. B.; Hass, J.; Marchenkov, A. N.; Conrad, E. H.; First, P. N.; de Heer, W. A. *Science* **2006**, *312*, 1191−1196.

(15) Stoller, M. D.; Park, S. J.; Zhu, Y. W.; An, J. H.; Ruoff, R. S. *Nano Lett.* **2008**, *8*, 3498−3502.

(16) Zhu, Y. W.; Murali, S.; Stoller, M. D.; Ganesh, K. J.; Cai, W. W.; Ferreira, P. J.; Pirkle, A.; Wallace, R. M.; Cychosz, K. A.; Thommes, M.; Su, D.; Stach, E. A.; Ruoff, R. S. *Science* **2011**, *332*, 1537−1541.

(17) El-kady, M. F.; Strong, V.; Dubin, S.; Kaner, R. B. *Science* **2012**, *335*, 1326−1330.

(18) Li, Y. Y.; Li, Z. S.; Shen, P. K. *Adv. Mater.* **2013**, *25*, 2474−2480.

(19) Wu, Z. S.; Wang, D. W.; Ren, W. C.; Zhao, J. P.; Zhou, G. M.; Li, F.; Cheng, H. M. *Adv. Funct. Mater.* **2010**, *20*, 3595−3602.

(20) Yu, G. H.; Hu, L. B.; Vosgueritchian, M.; Wang, H. L.; Xie, X.; McDonough, J. R.; Cui, X.; Cui, Y.; Bao, Z. N. *Nano Lett.* **2011**, *11*, 2905−2911.

(21) Xia, X. H.; Tu, J. P.; Mai, Y. J.; Chen, R.; Wang, X. L.; Gu, C. D.; Zhao, X. B. *Chem.—Eur. J.* **2011**, *17*, 10898−10905.

(22) Zhang, K.; Zhang, L. L.; Zhao, X. S.; Wu, J. S. *Chem. Mater.* **2010**, *22*, 1392−1401.

(23) Jeong, H. M.; Lee, J. W.; Shin, W. H.; Choi, Y. J.; Shin, H. J.; Kang, J. K.; Choi, J. W. *Nano Lett.* **2011**, *11*, 2472−2477.

(24) Wu, Z. S.; Winter, A.; Chen, L.; Sun, Y.; Turchanin, A.; Feng, X. L.; Müllen, K. *Adv. Mater.* **2012**, *24*, 5130−5135.

(25) Wen, Z. H.; Wang, X. C.; Mao, S.; Bo, Z.; Kim, H.; Cui, S. M.; Lu, G. H.; Feng, X. L.; Chen, J. H. *Adv. Mater.* **2012**, *24*, 5610−5616.

(26) Zhao, Y.; Hu, C. G.; Hu, Y.; Cheng, H. H.; Shi, G. Q.; Qu, L. T. *Angew. Chem., Int. Ed.* **2012**, *51*, 11371−11375.

(27) Li, Y. G.; Wu, Y. Y. *J. Am. Chem. Soc.* **2009**, *131*, 5851−5857.

(28) Li, X. H.; Kurasch, S.; Kaiser, U.; Antonietti, M. *Angew. Chem., Int. Ed.* **2012**, *51*, 9689−9692.

(29) NIST X-ray Photoelectron Spectroscopy (XPS) Database, Version 4.1, http://srdata.nist.gov/xps/.

(30) Puziy, A. M.; Poddubnaya, O. I.; Martínez-Alonso, A.; Suárez-García, F.; Tascón, J. M. D. *Carbon* **2002**, *40*, 1493−1505.

(31) Puziy, A. M.; Poddubnaya, O. I.; Martínez-Alonso, A.; Suárez-García, F.; Tascón, J. M. D. *Carbon* **2005**, *43*, 2857−2868.

(32) Puziy, A. M.; Poddubnaya, O. I.; Socha, R. P.; Gurgul, J.; Wisniewski, M. *Carbon* **2008**, *46*, 2113−2123.

(33) Ferrari, A. C.; Meyer, J. C.; Scardaci, V.; Casiraghi, C.; Lazzeri, M.; Mauri, F.; Piscanec, S.; Jiang, D.; Novoselov, K. S.; Geim, A. K. *Phys. Rev. Lett.* **2006**, *97*, 187401/1−187401/4.

(34) Ferrari, A. C.; Robertson, J. *Phys. Rev. B* **2000**, *61*, 14095−14107.